Journal of Materials Chemistry A

ROYAL SOCIETY OF CHEMISTRY

PAPER

View Article Online
View Journal | View Issue

Cite this: J. Mater. Chem. A, 2025, 13, 17720

A *meta*-linked isomer of ITIC: influence of aggregation patterns on open-circuit voltage in organic solar cells†

Kai Wang,[a] Seihou Jinnai, *[ab] Kaito Uesaka,[c] Akira Yamakata *[cde] and Yutaka Ie *[ab]

Received 8th January 2025
Accepted 23rd April 2025

DOI: 10.1039/d5ta00178a

rsc.li/materials-a

Improving the open-circuit voltage (V_{OC}) of organic solar cells (OSCs) remains an important challenge. While it is known that the energy levels at the donor/acceptor (D/A) interface affect the V_{OC}, the impact of aggregation patterns on the energy levels at the D/A interface has not been fully elucidated. Herein, we focus on **ITIC**, a widely used acceptor in OSCs, and designed a *meta*-linked isomer of **ITIC** (referred to as **im-ITIC**) to alter molecular symmetry and modify substitution arrangements. Concentration-dependent ^{1}H NMR spectra revealed that **im-ITIC** shows stronger aggregation behavior in solution. Single-crystal X-ray analysis showed that **im-ITIC** forms both tail-to-tail (J-aggregation) and face-to-face (H-aggregation) stacking modes, whereas **ITIC** exclusively forms tail-to-tail stacking. OSCs based on PBDB-T:**im-ITIC** showed a high V_{OC} value of 1.02 V, which is 0.12 V higher than that of those based on PBDB-T:**ITIC**. Time-resolved infrared measurements revealed the lifetime of free electrons for the pristine and blend films. The energy levels of the charge transfer state (E_{CT}) for PBDB-T:**im-ITIC**- and PBDB-T:**ITIC** OSCs were determined to be 1.57 and 1.39 eV, respectively, correlating with the V_{OC} values. Theoretical calculations indicated that pronounced H-aggregation in **im-ITIC** increases the E_{CT} compared with J-aggregation, contributing to the improved V_{OC}. This study underscores the critical impact of molecular aggregation patterns on energy alignment and V_{OC} enhancement, offering insights into molecular design for achieving high V_{OC} in OSCs.

Introduction

Organic solar cells (OSCs) have garnered increasing attention owing to their advantages, including cost-effectiveness, lightweight nature, flexibility, suitability for large-scale manufacturing, and wavelength-selective applications.[1–5] Significant progress in material design and device optimization has increased the power conversion efficiency (PCE) of single-junction OSCs up to 20%.[6–9] The photovoltaic performance of OSCs is determined by three key parameters: short-circuit current density (J_{SC}), the fill factor (FF), and open-circuit voltage (V_{OC}). Recent advancements, particularly in state-of-the-art fused-ring acceptors, have enabled J_{SC} and the FF to reach 85% of the Shockley–Queisser limit.[10,11] However, achieving high V_{OC} remains the primary challenge in the pursuit of high performance OSCs.

The V_{OC} of OSCs is primarily correlated with the energy level of the charge-transfer state (E_{CT}), where a hole resides in the donor (D) phase and an electron in the acceptor (A) phase at the D/A interface (Fig. 1a).[12,13] The E_{CT} is largely influenced by the energy offset between the highest occupied molecular orbital (HOMO) of the donor and the lowest unoccupied molecular orbital (LUMO) of the acceptor at the D/A interface.[14] While controlling the energy levels at the D/A interface is crucial for improving the V_{OC}, the complexity and variability of the morphologies at the D/A interface make it challenging to develop strategies for controlling the E_{CT} through molecular design.

The energy levels of organic semiconductors are affected by aggregation in the solid state and at the D/A interface.[15] In dimer models, it is well-known that these energy levels vary depending on the aggregation mode, such as J- and H-aggregation.[16–19] To investigate the influence of the aggregation patterns on the E_{CT} and V_{OC}, a W-shaped **ITIC** isomer, *i.e.* **im-ITIC**, was designed (Fig. 1b). **ITIC** is a representative acceptor in OSCs and belongs to C_{2h} symmetry, where bulky substituents are introduced on both

[a]The Institute of Scientific and Industrial Research (SANKEN), The University of Osaka, 8-1 Mihogaoka, Ibaraki, Osaka 567-0047, Japan. E-mail: jinnai@sanken.osaka-u.ac.jp; yutakaie@sanken.osaka-u.ac.jp

[b]Innovative Catalysis Science Division, Institute for Open and Transdisciplinary Research Initiatives (ICS-OTRI), The University of Osaka, 2-1 Yamadaoka, Suita, Osaka, 565-0871, Japan

[c]Graduate School of Natural Science & Technology, Okayama University, 3-1-1 Tsushima-naka, Okayama 700-8530, Japan. E-mail: yamakata@okayama-u.ac.jp

[d]Research Institute for Interdisciplinary Science, Okayama University, 3-1-1 Tsushima-naka, Okayama, 700-8530, Japan

[e]Institute for Aqua Regeneration, Shinshu University, 4-17-1 Wakasato, Nagano-shi, Nagano 380-8553, Japan

† Electronic supplementary information (ESI) available. See DOI: https://doi.org/10.1039/d5ta00178a

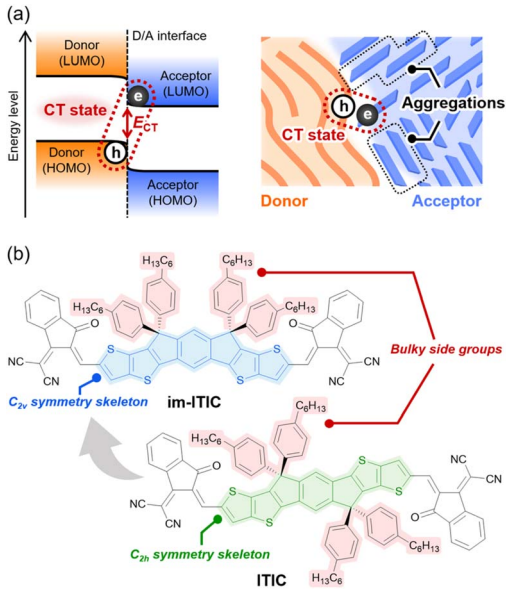

Fig. 1 (a) Schematics for the CT state at the D/A interface and (b) chemical structures of im-ITIC and ITIC.

sides of the fused polycyclic π-conjugated chain.[20] In contrast, **im-ITIC** exhibits C_{2v} symmetry, with bulky substituents on one side of the conjugated chain. As a result, the intermolecular interactions between **ITIC** and **im-ITIC** are expected to differ, leading to distinct stacking conformations in the solid state. In this study, we aimed to elucidate the influence of the molecular structures of **ITIC** and **im-ITIC** on their aggregation patterns and to investigate the relationship among the aggregation, E_{CT} at the D/A interface, and V_{OC} of OSCs.

Results and discussion

Synthesis and characterization

The synthetic route to **im-ITIC** is shown in Scheme 1. Compound **1** was prepared following a previously reported method.[21] Then, a Stille coupling reaction was carried out to give compound **2**. **im-IDTT** was synthesized *via* nucleophilic addition of the aryllithium and a cyclization reaction using H_2SO_4/AcOH. The formylation of **im-IDTT** afforded **im-IDTT-CHO**, which was then subjected to Knoevenagel condensation with 1-(dicyanomethylene)-3-indanone to give **im-ITIC**. The synthetic details, structural characterization, ^{1}H and ^{13}C NMR spectra, and high-resolution mass spectrometry data are provided in the (ESI†). As shown in Fig. S1,† thermogravimetric analysis (TGA) showed that **im-ITIC** exhibits good thermal stability with a decomposition temperature of 342 °C at a 5% weight loss.

The concentration-dependent ^{1}H NMR spectra of **im-ITIC** in deuterated chloroform ($CDCl_3$) solution were measured to investigate the aggregation behavior. As shown in Fig. 2 and S2,† certain protons in the aromatic region shift significantly with increasing concentration. Notably, the protons in the central ring (H_a), the thiophene ring (H_c), and the vinyl group (H_d), located on the side opposite to alkyl groups, shift to a higher field. In contrast, the shifts of the H_b protons, which are on the same side as the alkyl groups, are less pronounced. This result indicates that **im-ITIC** exhibits aggregation behavior on the side opposite to bulky substituents, which differs markedly from the J-aggregation pattern typically seen in **ITIC** (see Fig. S3† and other representative NFAs).

Theoretical investigation

To gain insight into the effect of isomeric structure on electronic states, density functional theory (DFT) calculations were performed using Gaussian 16 software at the B3LYP/6-31G(d,p) level. As shown in Fig. S4,† the conjugated backbone of **im-ITIC** showed a planar configuration, similar to that of **ITIC**. Additionally, **im-ITIC** exhibits a significantly larger dipole moment (μ) of 12.14 D compared with 0.04 D for **ITIC** due to the C_{2v} symmetry of its backbone. The distributions of the HOMO and the LUMO, along with their energy levels, are summarized in Fig. S5.† Both **im-ITIC** and **ITIC** exhibit similar frontier molecular orbital distributions, with **im-ITIC** featuring a deeper

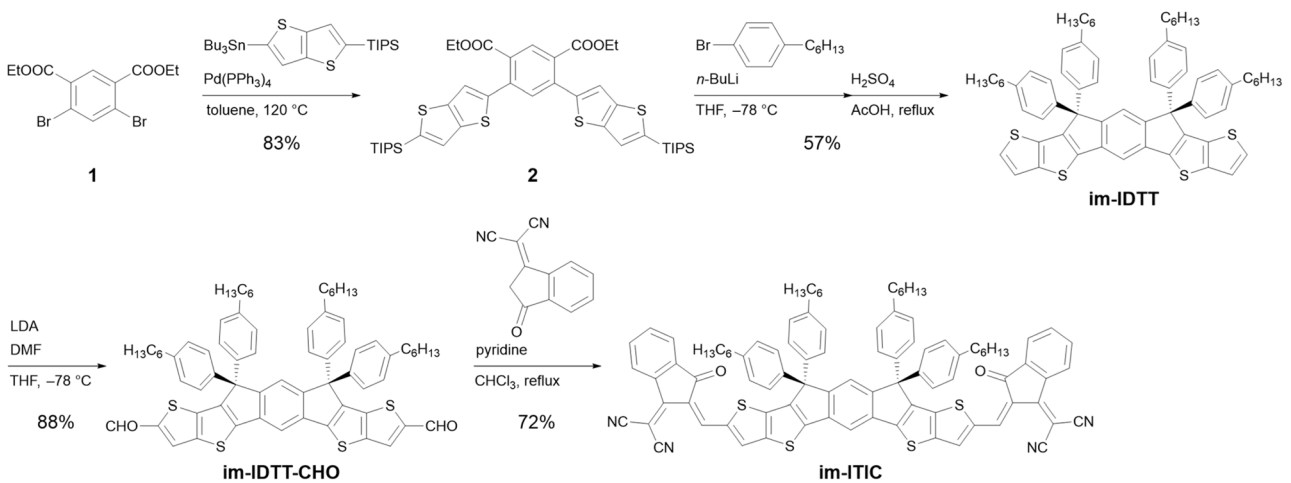

Scheme 1 Synthetic route to im-ITIC.

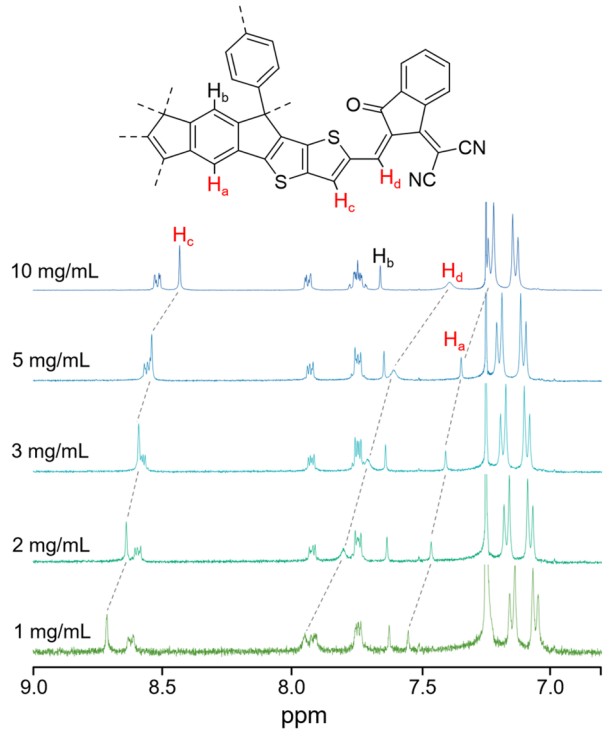

Fig. 2 Concentration-dependent ^{1}H NMR spectra of the aromatic region for **im-ITIC** in $CDCl_3$ at 20 °C. The entire spectra are given in Fig. S2.†

HOMO energy level of −5.57 eV, compared with −5.46 eV for **ITIC**. The LUMO energy level of **im-ITIC** shifts upward to −3.24 eV compared with −3.35 eV for **ITIC**.

Electrochemical and photophysical properties

The electrochemical properties of **im-ITIC** and **ITIC** were investigated using differential pulse voltammetry (DPV) in *o*-dichlorobenzene/acetonitrile (CH_3CN) (5/1) solutions containing 0.1 M tetrabutylammonium hexafluorophosphate ($TBAPF_6$) as a supporting electrolyte. The potentials were calibrated by a ferrocene/ferrocenium (Fc/Fc^+) redox couple as an internal standard. As shown in Fig. S6,† these isomers exhibited two reduction and oxidation peaks in cathodic and anodic sweeps, respectively. The first reduction potential (E_{red}) of **im-ITIC** was 0.07 V more negative than that of **ITIC**, while the first oxidation potential (E_{ox}) was 0.11 V more positive. Based on the redox potentials, the LUMO energy level (E_{LUMO}) and HOMO energy level (E_{HOMO}) of **im-ITIC** and **ITIC** were determined to be −5.65/−3.79 and −5.54/−3.86 eV, respectively. These potentials of **im-ITIC** and **ITIC** are summarized in Table 1. The relative energy levels of **im-ITIC** and **ITIC** based on the DPV were qualitatively consistent with the DFT results shown in Fig. S5.†

The UV-vis absorption spectra in chloroform solutions are shown in Fig. 3a **im-ITIC** showed a blue-shifted absorption band compared with **ITIC**, and their absorption maxima (λ_{max}^{sol}) were at 621 and 679 nm, respectively. The molar absorption coefficient (ε_{sol}) for **im-ITIC** (1.62×10^5 L mol^{-1} cm^{-1}) is almost comparable to that of **ITIC** (1.76×10^5 L mol^{-1} cm^{-1}), which is consistent with their oscillator strength in the DFT results (Fig. S5†). In the film state, the maximum absorption peaks (λ_{max}^{film}) of **im-ITIC** and **ITIC** are located at 636 and 699 nm. Based on the onset wavelength of the absorption spectra, the optical energy gaps (E_g^{opt}) for **im-ITIC** and **ITIC** were estimated to be 1.76 and 1.62 eV, respectively.

Table 1 Physical properties of **im-ITIC** and ITIC

Compounds	λ_{max}^{sol} [a] (nm)	λ_{max}^{film} (nm)	λ_{onset}^{film} (nm)	E_g^{opt} [b] (eV)	E_{HOMO} [c] (eV)	E_{LUMO} [c] (eV)	IE [d] (eV)	EA [e] (eV)
im-ITIC	621	636	704	1.76	−5.65	−3.79	5.97	3.85
ITIC	679	697	765	1.62	−5.54	−3.86	5.88	3.87

[a] In chloroform. [b] E_g^{opt} was calculated using $1240/\lambda_{onset}^{film}$. [c] Determined *via* DPV in *o*-DCB/CH_3CN containing 0.1 M of $TBAPF_6$. [d] Estimated using PYS. [e] Estimated using LEIPS.

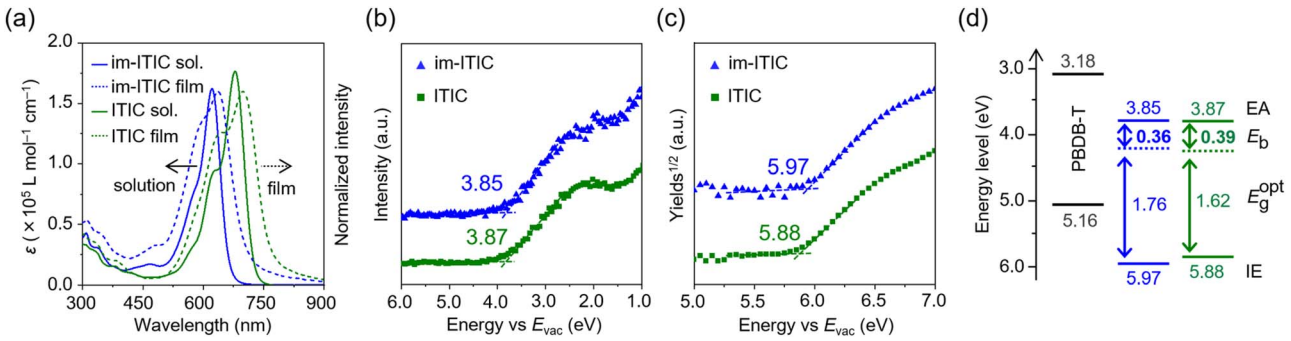

Fig. 3 (a) UV-vis absorption spectra, (b) LEIPS, and (c) PYS of **im-ITIC**, **ITIC** in pristine films. (d) Energy level diagram of **im-ITIC** (blue), **ITIC** (green), and **PBDB-T** (black).

To investigate the electron affinity (EA) and ionization energy (IE) of **im-ITIC** and **ITIC**, low-energy inverse photoemission spectroscopy (LEIPS)[22,23] and photoelectron yield spectroscopy (PYS)[24] were conducted. As shown in Fig. 3b and c, the IE/EA values for **im-ITIC** and **ITIC** are determined to be 5.97/3.85 and 5.88/3.87 eV, respectively. Compared with the E_{HOMO} and E_{LUMO} values in solution, the differences in IE and EA values for **im-ITIC** and **ITIC** became smaller. In particular, the difference in EA is only 0.02 eV. Generally, intermolecular interactions cause shallow E_{HOMO} and deep E_{LUMO}, resulting in narrowing of the HOMO–LUMO energy gap. In this context, **im-ITIC** possibly has larger intermolecular interactions in the solid state compared with **ITIC**. The resulting energy diagram along with a typical donor of PBDB-T (CAS registry #1415929-80-4) are summarized in Fig. 3d. Since the IE and EA offsets were larger than 0.3 eV with respect to PBDB-T, **im-ITIC** and **ITIC** possess enough driving force for charge separation.[25] Based on the IE, EA, and E_g^{opt} values, the exciton binding energies (E_b) of **im-ITIC** and **ITIC** were estimated to be 0.36 and 0.39 eV, respectively. This result indicated that the Coulomb attraction force of excitons in **im-ITIC** is smaller than that in **ITIC**, which is advantageous for photo-charge generation.[25–27]

Molecular structure and packing diagram

To investigate the molecular structure and packing diagram of **im-ITIC** in the solid state, single-crystal X-ray diffraction was performed. The single crystal was grown by the vapor diffusion method from chloroform/methanol (see details in the ESI†). As shown in Fig. 4a, the molecular skeleton of **im-ITIC** adopts a W-shaped geometry and exists in two configurations: one with a generally planar structure (configuration A) and another with twisted terminal DCI groups, featuring a torsion angle of 17.8° (configuration B). As shown in Fig. 4b and c, **im-ITIC** has a similar twisted 2D brickwork structure to that of **ITIC**, which self-assembled into 3D crystal lattices through side-chain interactions and hydrogen bonding. For **im-ITIC**, the intermolecular distance between π–π stacked molecules is approximately 3.40 Å. As shown in Fig. 4c, **ITIC** exclusively forms tail-to-tail J-aggregates. In contrast, **im-ITIC** showed four distinct binary aggregates, including two face-to-face H-aggregates and two tail-to-tail J-aggregates. The ratio of H-aggregates to J-aggregates is approximately 1 : 1, which differs significantly from the aggregation behavior of **ITIC**.

Based on these dimer structures of **im-ITIC** and **ITIC**, we calculated the energy levels for these aggregates. As shown in Fig. S7,† the LUMO energy levels of **im-ITIC-Ja** are nearly identical to those of **ITIC-Ja** and **ITIC-Jb**. In contrast, the LUMO energy levels of the H-aggregates (**im-ITIC-Ha** and **im-ITIC-Hb**) are relatively shallower than those of the J-aggregates (**im-ITIC-Ja** and **im-ITIC-Jb**).[28,29] These phenomena indicate that the LUMO energy level of **im-ITIC** is influenced by its stacking mode. Conversely, the HOMO energy levels of H-aggregates and J-aggregates for **im-ITIC** are less affected because the electron clouds of HOMO are localized in the central part of **im-ITIC**. These trends are in good agreement with the experimentally determined IE/EA results.

Photovoltaic characteristics

To investigate the photovoltaic characteristics of **im-ITIC**, we fabricated OSCs with an inverted configuration of ITO/ZnO/PBDB-T:**im-ITIC**/MoO_3/Ag (Fig. S8†).[30] Fig. 5a shows the *J*–*V* characteristics of the OSCs under an air mass of 1.5 G using a solar simulator lamp (100 mW cm^{-2}), and the key OSC parameters are summarized in Table 2. During the optimization process of **im-ITIC**-based OSCs, the inclusion of additives such as 1,8-diiodooctane (DIO) and 1-chloronaphthalene (CN) was found to affect the V_{OC} and J_{SC} of the OSCs.[17,31] The J_{SC} and external quantum efficiency (EQE) of OSCs increased by the addition of CN and DIO (Fig. 5b). Notably, the addition of DIO increased the V_{OC} from 0.95 to 1.02 V. As shown in Fig. S9,† the UV-vis absorption spectrum of DIO-processed **im-ITIC** films showed a shoulder peak around 605 nm, which can be attributed to the absorption of H-aggregates.[17,28] This result implies that the H-aggregation of **im-ITIC** contributed to the increased V_{OC}.

The surface morphologies of the PBDB-T:**im-ITIC** films were investigated using atomic force microscopy (AFM). As shown in Fig. S10,† all films exhibit similar surface morphology and roughness but have a smoother surface compared with ITIC. To investigate the crystallinity and molecular arrangement of the PBDB-T:**im-ITIC** films, X-ray diffraction (XRD) measurements were performed. As shown in Fig. S11† the diffraction intensities in the out-of-plane profiles become prominent when CN and DIO were added, indicating that the addition of CN and DIO improved the crystallinity of the blend films.

The electron and hole mobilities (μ_e and μ_h) of the PBDB-T:**im-ITIC** films with different additives were investigated using the space-charge-limited-current (SCLC) model, and the results are summarized in Table S1 and Fig. S12a and S12b.† (ref. 32–34) The μ_h value of 2.5×10^{-5} cm^2 V^{-1} s^{-1} was the same for all the conditions. On the other hand, the μ_e was slightly improved from 9.2×10^{-6} to 9.7×10^{-6} and 9.9×10^{-6} cm^2 V^{-1} s^{-1} by the addition of CN and DIO respectively, which contributed to the improved J_{SC} and FF of OSCs.

The photocurrent density (J_{ph}) against effective applied voltage (V_{eff}) for PBDB-T:**im-ITIC** based OSCs is plotted in Fig. S12c.† (ref. 35 and 36) The J_{ph} of PBDB-T:**im-ITIC** devices processed with CN and DIO exhibited saturation. In contrast, the blend film without additive showed no distinct J_{ph} saturation, possibly due to the contribution of non-geminate recombination. Based on the ratio of J_{ph} to the saturation current density (J_{sat}), the exciton dissociation probabilities ($P(E,T)$) for CN- and DIO-processed OSCs were calculated to be 93%, and 96%, respectively. To investigate the non-geminate recombination in blend films, the J_{SC} against light intensity (P_{light}) was measured. As shown in Fig. S12d,† the exponential factors (α) for the blend films without additive and for CN- and DIO-processed films were determined to be 0.87, 0.93 and 0.99, respectively. The α value close to 1.00 observed for the DIO-processed OSC indicates negligible non-geminate recombination losses. In contrast, the lower α value for the blend film without additive suggests a significant contribution of non-

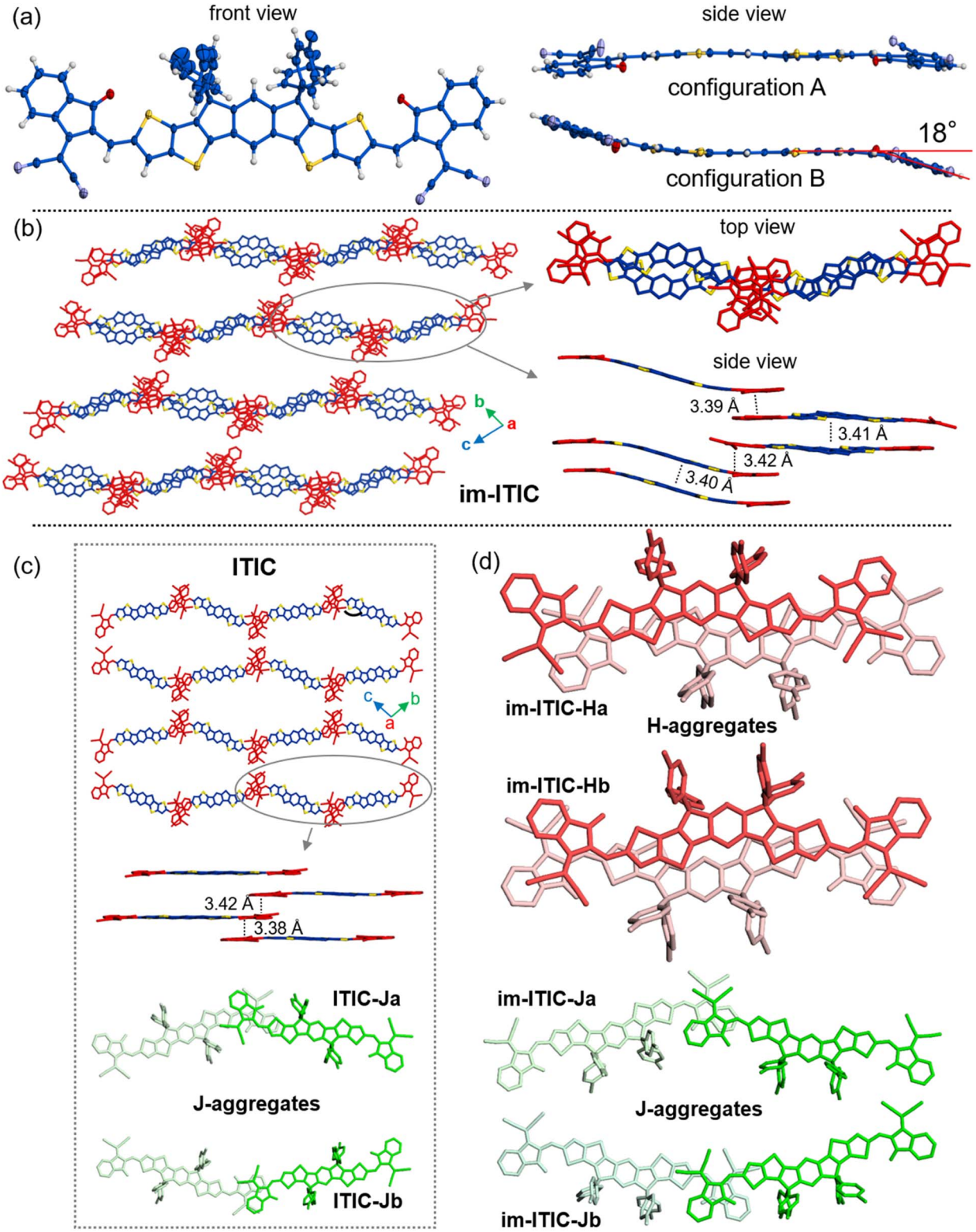

Fig. 4 Single-crystal structures of **im-ITIC** and **ITIC**. (a) Configurations of the mono-molecule of **im-ITIC** in single crystallographic structures from top and side views (d_{S-O} = the length of the S···O interaction). (b) Single-crystal packing diagrams for **im-ITIC** from the top and side views. (c) Single crystal packing diagrams and aggregation pairs for **ITIC**. (d) Different intermolecular aggregation pairs for **im-ITIC**. Details of single crystal data are summarized in Table S3.† All the side chains are removed or simplified for clarity. The single crystal data of **ITIC** were obtained from the literature.[51]

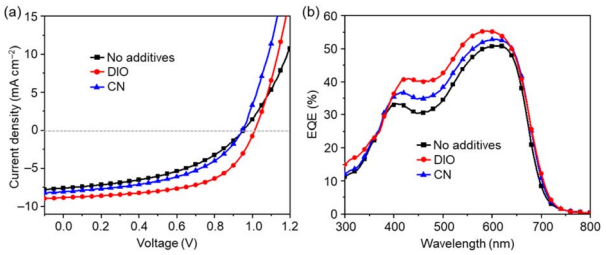

Fig. 5 (a) J–V curves and (b) EQE spectra of PBDB-T:**im-ITIC** with different additives.

geminate recombination. These trends are consistent with the results shown in Fig. S12c.†

To investigate the origin of the high V_{OC} in the DIO-processed films, the E_{CT} energy was determined from the normalized external quantum efficiency (EQE) spectra (Fig. S13†).[37] As a result, the E_{CT} of the DIO-processed PBDB-T:**im-ITIC** film (1.57 eV) was estimated to be higher than that of the CN-processed film (1.54 eV) and the blend film without additives (1.54 eV). A positive correlation was found between the estimated E_{CT} and the V_{OC} of OSCs.

The limited PCE of **im-ITIC**-based devices compared with the **ITIC**-based device is primary due to the reduced J_{SC} (Fig. S14a and S14b†), which can be attributed to the significant overlap of the absorption bands between **im-ITIC** and PBDB-T (Fig. S15†). Notably, the V_{OC} of the **im-ITIC**-based device reached a high value of 1.02 V, which is 0.12 V higher than that of the **ITIC**-based device. As we discussed above, **im-ITIC** and **ITIC** exhibited similar EA values in their pristine films. Therefore, the difference in V_{OC} between the **im-ITIC**- and **ITIC**-based OSCs would be attributed to the energy state at the D/A interface, specifically E_{CT}, rather than the intrinsic energy levels of the acceptors. In fact, the E_{CT} value of the PBDB-T:**ITIC** film was determined to be 1.39 eV (Fig. S14c†).

Time-resolved infrared (TR-IR) absorption spectroscopy

To investigate the photo-charge generation in pristine and blend films for **im-ITIC** and **ITIC**, time-resolved infrared (TR-IR) absorption measurements were employed. This method enables detailed analysis of charge separation processes as well as the decay dynamics of the free carriers. In particular, the vibrational frequency of the cyano group, which is introduced as an electron-accepting group in NFAs, shifts to lower

Table 2 OSC characteristics of **im-ITIC** and **ITIC**

Active layer	Additive	PCE (%)	J_{SC} (mA cm^{-2})	V_{oc} (V)	FF (%)	EQE$_{max}$ (%)	E_{CT} (eV)
PBDB-T:**im-ITIC**	DIO[a]	5.13 (4.88 ± 0.37)	9.06 (8.84 ± 0.22)	1.02 (1.01 ± 0.01)	57 (56 ± 1)	56.2	1.57
PBDB-T:**im-ITIC**	CN[a]	3.74 (3.62 ± 0.12)	8.10 (7.98 ± 0.13)	0.95 (0.95 ± 0.01)	49 (56 ± 1)	52.7	1.54
PBDB-T:**im-ITIC**	—	3.25 (3.18 ± 0.06)	7.81 (7.71 ± 0.12)	0.95 (0.95 ± 0.01)	45 (44 ± 1)	50.8	1.54
PBDB-T:**ITIC**	DIO[b]	8.62 (8.41 ± 0.13)	14.73 (14.33 ± 0.28)	0.90 (0.90 ± 0.01)	65 (65 ± 1)	72.2	1.39

[a] 1 vol% concentration was added. [b] 0.5 vol% concentration was added.

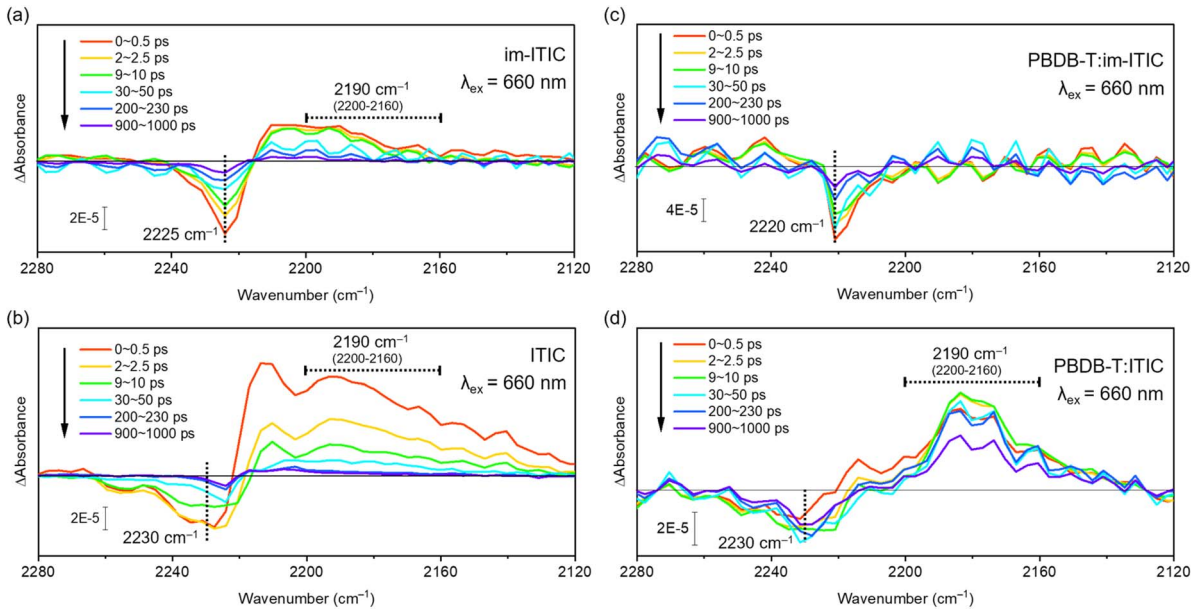

Fig. 6 Differential vibrational spectra of cyano groups in NFAs after pump pulse irradiation. Pristine (a) **im-ITIC** and (b) **ITIC** films are photoexcited by a 660 nm pump pulse. Additionally, the NFA domain in the blend film with PBDB-T is photoexcited by the same 660 nm pump pulse (panels c–d).

wavenumbers with increasing electron density. This property allows the investigation of intra- and intermolecular charge transfer processes in NFAs.[38–40]

First, we measured the TR-IR absorption spectra in the cyano stretching region, as shown in Fig. 6. The results showed that a negative peak at 2230 cm^{-1} and a positive peak between 2200 and 2160 cm^{-1} appeared upon 660 nm pump pulse irradiation (Fig. 6b). These peaks are assigned to ground-state bleaching of the cyano stretching mode, an S_1 state formed by intramolecular charge transfer in **ITIC**, and an anionic **ITIC** molecule generated by intermolecular charge separation, respectively.[38–40] These results indicate that intramolecular and intermolecular charge transfer occurs even in **ITIC** films upon photoirradiation (Fig. 6b). In the case of the **im-ITIC** film, a negative peak at 2225 cm^{-1} and a positive peak between 2200 and 2160 cm^{-1} similarly appeared upon pump pulse irradiation (Fig. 6a). These results confirm that the intermolecular charge transfer also takes place in the **im-ITIC** pristine film.

Similar TR-IR measurements were performed on the PBDB-T:**ITIC** and PBDB-T:**im-ITIC** blend films. As shown in Fig. 6d, when **ITIC** was blended with PBDB-T, the absorption intensity at 2230 cm^{-1} (S_1 state) becomes weaker, while the absorption between 2200 and 2160 cm^{-1} strengthens significantly, highlighting a distinct change in the spectral response. These results imply that the formation of heterojunctions with the donor promotes charge separation and increases the number of **ITIC** anions. On the other hand, ground-state bleaching was observed at 2220 cm^{-1} for the PBDB-T:**im-ITIC** blend film, although the positive signals were found to be negligible (Fig. 6c). While cationic **im-ITIC** are expected to induce a blue shift in the CN vibration, their oscillator strength is weak, making them undetectable.[38] However, since the formation of cationic states reduces the population of neutral molecules, they contribute to the appearance of the bleaching signal. The ground-state bleaching in **im-ITIC** suggests that electrons are not localized within the molecules to form an anionic state; instead, they are released from the molecules, resulting in the formation of free electrons.

The formation of free electrons can be confirmed by tracking the background absorption in the mid-infrared region. We have reported that free electrons excited in the **ITIC** layer give structures with broad absorption in the entire mid-IR region from 4000 to 1000 cm^{-1}, which is attributed to the intraband transition of free electrons.[38,41–43] In the case of **im-ITIC**, the broad IR absorption was also observed upon 660 nm pump pulse irradiation, as in the case of **ITIC** (Fig. S16a and S16b†). These results suggest that free electrons are also generated in the **im-ITIC** pristine film.

The decay dynamics of free electrons generated in **ITIC** and **im-ITIC** pristine films are shown in Fig. 7a and b. For both acceptors, the absorption at 2050 cm^{-1} increases immediately after photoexcitation and decays monotonically. Notably, **im-ITIC** exhibited a longer lifetime than **ITIC** in the time region of 0–1000 ps. This difference in lifetimes is considered to be due to the smaller E_b of **im-ITIC**, which reduced the Coulomb attraction force of electron–hole pairs in **im-ITIC** and suppressed charge recombination.

We also analyzed the decay dynamics for the PBDB-T:**im-ITIC** and PBDB-T:**ITIC** blend films. As in the case of **ITIC** and **im-ITIC** pristine films, the excitation of acceptors in the blend film causes broad IR absorption (Fig. S16c and S16d†), indicating that free electrons were also observed in the blend films.

The temporal profiles of the transient absorption at 2050 cm^{-1} further provided detailed information about the formation and the decay processes of the free electrons (Fig. 7c and d). As shown in Fig. 7c, the absorption intensity of free electrons for **ITIC** gradually increases in 0–10 ps. This result suggests that the charge separation is facilitated by the hole-transfer from the excited **ITIC** to the PBDB-T layer at the D/A interface. In contrast, **im-ITIC** showed an immediate increase in free carrier absorption after photoexcitation. This result shows that the hole transfer from **im-ITIC** to PBDB-T is much

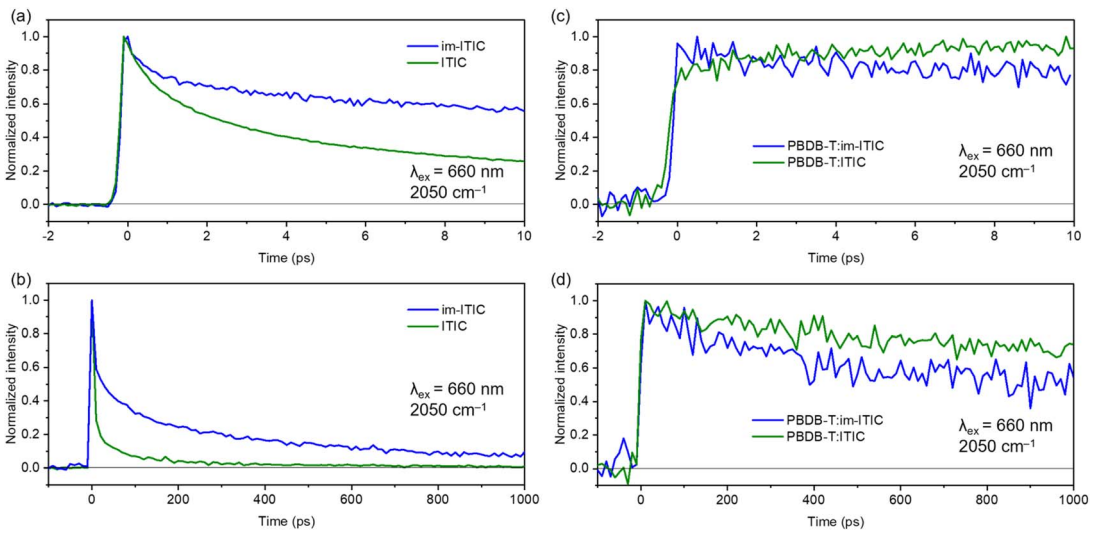

Fig. 7 Time profiles of free electrons in pristine ITIC and im-ITIC films (a & b) and in their blend films with PBDB-T (c & d). These profiles were obtained by photoexciting the NFA domain with a 660 nm pump pulse and measuring the transient absorption at 2050 cm^{-1}.

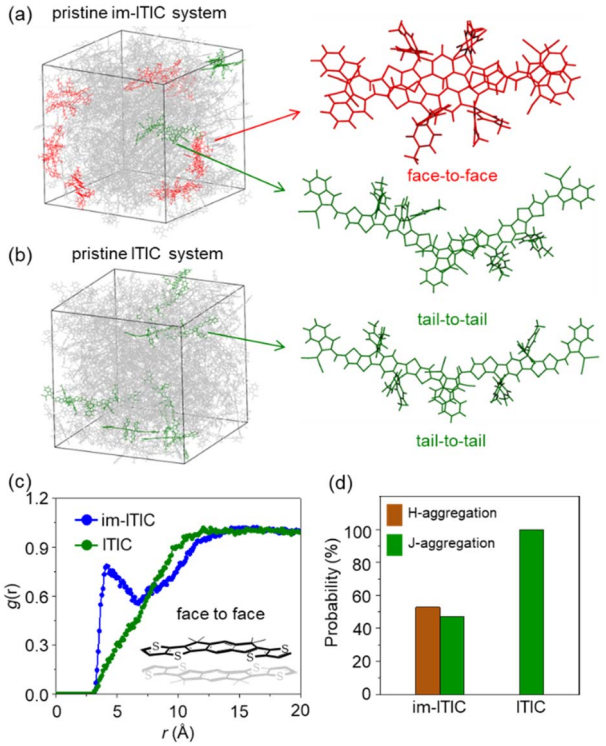

Fig. 8 (a) and (b) Snapshots (left) and examples of stacking modes (right) from the MD results of im-ITIC and ITIC based pristine systems. (c) Radial distribution function data for pristine systems. (d) Probability of different aggregations in pristine systems. In the snapshots, face-to-face and tail-to-tail aggregations are colored red and green, respectively.

faster compared with **ITIC**. However, the free carrier lifetime of **im-ITIC** was found to be shorter than that of **ITIC** (Fig. 7d). This is the opposite trend in pristine films where the lifetime of free electrons is longer in **im-ITIC** than in **ITIC**. These results align well with the experimental results of the OSC characteristics showing that PBDB-T:**ITIC** exhibits higher J_{SC} values than that of PBDB-T:**im-ITIC**.

Molecular-dynamics simulations

To understand the origin of difference in V_{OC}, molecular-dynamics (MD) simulations of **im-ITIC** and **ITIC** were carried out (see details in the ESI†).[44–46] Snapshots of the MD simulations for **im-ITIC** and **ITIC** are shown in Fig. 8a and b, and that for blend states with PBDB-T fragment are shown in Fig. S17a and S17b.† **ITIC** showed only tail-to-tail stacking between its terminal groups. In contrast, **im-ITIC** exhibited both H-aggregation and J-aggregation behaviors. These results are consistent with the crystal packing structures of **ITIC** and **im-ITIC** (Fig. 4). The above results are statistically shown in Fig. 8c and S16c,† where the radial distribution functions (RDFs) indicate the probability of finding a group some distance away from a reference group, with a higher $g(r)$ peak pointing to a larger packing density at a given distance.[47,48] It is significant that **im-ITIC** shows an evident peak around 4 Å in both pristine and blend states when considering the face-to-face stacking. The probability of different aggregation modes also clearly demonstrates the stacking differences between **im-ITIC** and **ITIC** (Fig. 8d and S16d†).

Further, MD simulations for **im-ITIC** in pristine and blend states with different additives were also performed to understand the effect of additives on the molecular packing. As shown in Fig. S18,† the addition of DIO significantly increases the probability of face-to-face stacking in pristine **im-ITIC** systems. This phenomenon is also observed in blend systems (Fig. S19†). As shown in Fig. S18c and S19c,† a distinct peak at around 4 Å is present between CN and **im-ITIC**, whereas no such peak was observed between DIO and **im-ITIC**. This result indicates that DIO does not form intermolecular interactions with **im-ITIC**, thereby increasing the possibility of face-to-face stacking of **im-ITIC** compared with CN. As a result, the use of DIO additives contributed to enhancing the H-aggregation behavior of **im-ITIC**, which is a critical factor for achieving high V_{OC} values in OSCs.

Excited state analysis

To further understand how H-aggregation increases V_{OC}, we performed time-dependent DFT (TD-DFT) calculations using

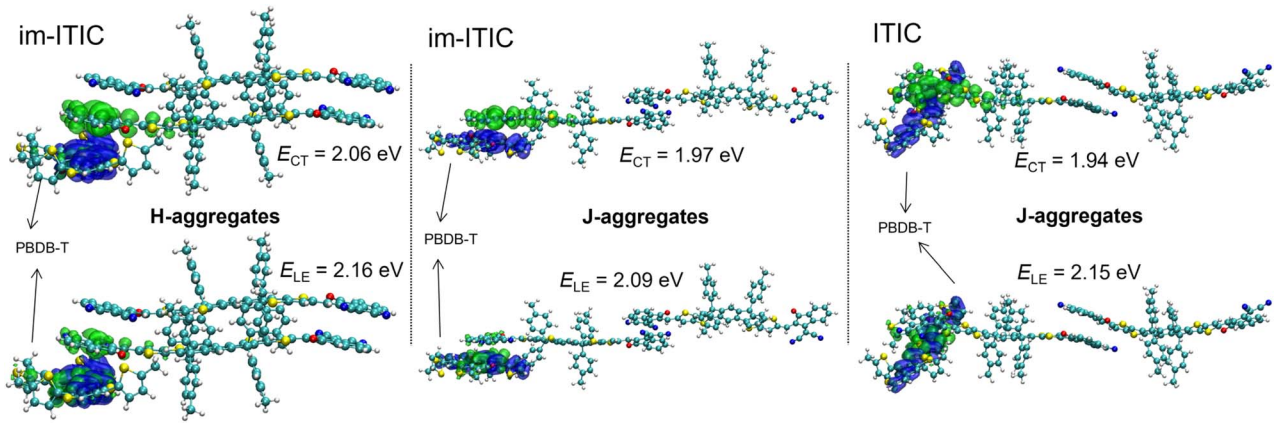

Fig. 9 Distributions of the hole (blue) and electron (green) for different excited states of different aggregates of im-ITIC. TD-DFT calculations were performed using the ωB97XD/6-31G(d,p) method on the molecular clusters from MD simulations.

the ωB97XD/6-31G(d,p) method on D:A clusters with different stacking modes from MD simulations.[39,47] Fig. 9 displays the hole and electron distributions for the lowest CT and localized excited (LE) states in various aggregates between **im-ITIC**/**ITIC** and the PBDB-T fragment. The E_{CT} values for H- and J-aggregates for **im-ITIC**-based clusters were calculated to be 2.06 and 1.97 eV, respectively. The E_{CT} value for the J-aggregate of the **ITIC**-based cluster had a slightly lower value of 1.94 eV. These results indicate that J-aggregation produces similar CT states between **im-ITIC** and **ITIC**. In contrast, H-aggregation in **im-ITIC** significantly raises the E_{CT} at the D/A interface. In addition, the energy offset (ΔE_{LE-CT}) between E_{CT} and E_{LE} for these clusters were calculated to be 0.10, 0.12 and 0.21 eV, respectively, indicating that H-aggregation possibly contributes to reducing the energy loss.[49,50] Thus, we conclude that the H-aggregation in **im-ITIC** raises the overall energy level of the CT state in OSCs, achieved through a molecular design that incorporates steric hindrance on only one side of the molecule.

Conclusions

To investigate the impact of aggregation behavior on V_{OC}, we designed **im-ITIC** with C_{2v} symmetry, arranging all the side chains on one side of **ITIC**. Concentration-dependent ^{1}H NMR spectra of **im-ITIC** exhibit aggregation behavior in solution. LEIPS measurements revealed that EA values for **im-ITIC** and **ITIC** pristine films were almost identical to each other. Based on the IE, EA, and E_g^{opt} values, the E_b values of **im-ITIC** and **ITIC** were estimated to be 0.36 and 0.40 eV, respectively. Single-crystal X-ray diffraction analysis revealed that **im-ITIC** exhibits H- and J-aggregates in the packing diagram. The PBDB-T:**im-ITIC**-based OSC showed a higher V_{OC} of 1.02 V compared with that of PBDB-T:**ITIC** (0.90 V). The V_{OC} of PBDB-T:**im-ITIC** was influenced by the choice of additives, showing higher V_{OC} when DIO was employed. The E_{CT} values of the PBDB-T:**im-ITIC** and PBDB-T:**ITIC** films were estimated to be 1.57 and 1.39 eV, respectively, demonstrating a positive correlation with the V_{OC} values of OSCs. TR-IR measurements revealed that the lifetime of free carriers in the pristine **im-ITIC** film was longer than that of **ITIC**, while the lifetime of the PBDB-T:**im-ITIC** blend film was found to be shorter than that of the PBDB-T:**ITIC** film. These results align with the E_b values in pristine film and the J_{SC} values of the blend films. Through MD simulations and TD-DFT calculations, we found that the H-aggregation behavior of **im-ITIC** substantially increases the E_{CT} energy level at the D:A interface compared with J-aggregates, thereby improving V_{OC}. This study demonstrated that the aggregation behavior induced by the molecular structure of acceptors influences the E_{CT} and the V_{OC} in OSCs, offering valuable insights for designing high-performance nonfullerene acceptors.

Data availability

The data supporting this article have been included as part of the ESI.†

Author contributions

All the authors have given approval to the final version of the manuscript.

Conflicts of interest

There are no conflicts to declare.

Acknowledgements

This work was supported by the Japan Society for the Promotion of Science (20H02814, 20H05841, 20KK0123, 23K17947, 20K15352, 23H02064, 20H05838, 24H00485, and 24H00482), New Energy and Industrial Technology Development Organization (215002 48-0), Japan Science and Technology Agency (JPMJMI22I1, JPMJSF23B3, and JPMJCR20R1), and Mitsubishi Foundation (202310004). We thank the Comprehensive Analysis Center (CAC), SANKEN, for assistance in performing elemental analyses and obtaining high-resolution mass spectra.

Notes and references

1 S. M. Lu, S. Amaducci, S. Gorjian, M. Haworth, C. Hägglund, T. Ma, S. Zainali and P. E. Campana, *Joule*, 2024, **8**, 2483–2522.
2 S. Chatterjee, S. Jinnai and Y. Ie, *J. Mater. Chem. A*, 2021, **9**, 18857–18886.
3 S. Chatterjee, N. Shimohara, T. Seo, S. Jinnai, T. Moriyama, M. Saida, K. Omote, K. Hama, Y. Iimuro, Y. Watanabe and Y. Ie, *Mater. Today Energy*, 2024, **45**, 101673.
4 S. Jinnai, N. Shimohara, K. Ishikawa, K. Hama, Y. Iimuro, T. Washio, Y. Watanabe and Y. Ie, *Faraday Discuss.*, 2024, **250**, 220–232.
5 S. Jinnai, A. Oi, T. Seo, T. Moriyama, M. Terashima, M. Suzuki, K.-i. Nakayama, Y. Watanabe and Y. Ie, *ACS Sustain. Chem. Eng.*, 2023, **11**, 1548–1556.
6 L. Zhu, M. Zhang, Z. Zhou, W. Zhong, T. Hao, S. Xu, R. Zeng, J. Zhuang, X. Xue, H. Jing, Y. Zhang and F. Liu, *Nat. Rev. Electr. Eng.*, 2024, **1**, 581–596.
7 S. Guan, Y. Li, C. Xu, N. Yin, C. Xu, C. Wang, M. Wang, Y. Xu, Q. Chen, D. Wang, L. Zuo and H. Chen, *Adv. Mater.*, 2024, **36**, 2400342.
8 Y. Sun, L. Wang, C. Guo, J. Xiao, C. Liu, C. Chen, W. Xia, Z. Gan, J. Cheng, J. Zhou, Z. Chen, J. Zhou, D. Liu, T. Wang and W. Li, *J. Am. Chem. Soc.*, 2024, **146**, 12011–12019.
9 L. Zhu, M. Zhang, G. Q. Zhou, Z. Y. Wang, W. K. Zhong, J. X. Zhuang, Z. C. Zhou, X. Y. Gao, L. X. Kan, B. N. Hao, F. Han, R. Zeng, X. N. Xue, S. J. Xu, H. Jing, B. Xiao, H. M. Zhu, Y. M. Zhang and F. Liu, *Joule*, 2024, **8**, 3153–3168.
10 W. Shockley and H. J. Queisser, *J. Appl. Phys.*, 1961, **32**, 510–519.
11 Y. B. Kong, H. Z. Chen and L. J. Zuo, *Adv. Funct. Mater.*, 2024, 2413864.
12 C. Deibel, T. Strobel and V. Dyakonov, *Adv. Mater.*, 2010, **22**, 4097–4111.

13 X. Y. Zhu, Q. Yang and M. Muntwiler, *Acc. Chem. Res.*, 2009, **42**, 1779–1787.
14 D. He, F. W. Zhao, C. R. Wang and Y. Z. Lin, *Adv. Funct. Mater.*, 2022, **32**, 2111855.
15 Y. H. Deng, W. Yuan, Z. Jia and G. Liu, *J. Phys. Chem. B*, 2014, **118**, 14536–14545.
16 K. Cai, J. J. Xie, D. Zhang, W. J. Shi, Q. F. Yan and D. H. Zhao, *J. Am. Chem. Soc.*, 2018, **140**, 5764–5773.
17 Q. Q. Zhao, H. J. Lai, H. Chen, H. Li and F. He, *J. Mater. Chem. A*, 2021, **9**, 1119–1126.
18 S. Li, L. Y. Fu, X. X. Xiao, H. Geng, Q. Liao, Y. Liao and H. B. Fu, *Angew. Chem., Int. Ed.*, 2021, **60**, 18059–18064.
19 J. H. Kim, T. Schembri, D. Bialas, M. Stolte and F. Würthner, *Adv. Mater.*, 2022, **34**, 2104678.
20 Y. Z. Lin, J. Y. Wang, Z. G. Zhang, H. T. Bai, Y. F. Li, D. B. Zhu and X. W. Zhan, *Adv. Mater.*, 2015, **27**, 1170–1174.
21 Y. Shi, T. Suguri, C. Dohi, H. Yamada, S. Kojima and Y. Yamamoto, *Chem.–Eur. J.*, 2013, **19**, 10672–10689.
22 H. Yoshida, *Chem. Phys. Lett.*, 2012, **539**, 180–185.
23 H. Yoshida, *J. Electron Spectrosc. Relat. Phenom.*, 2015, **204**, 116–124.
24 J. P. Yang, F. Bussolotti, S. Kera and N. Ueno, *J. Phys. D: Appl. Phys.*, 2017, **50**, 423002.
25 J. Liu, S. S. Chen, D. P. Qian, B. Gautam, G. F. Yang, J. B. Zhao, J. Bergqvist, F. L. Zhang, W. Ma, H. Ade, O. Inganäs, K. Gundogdu, F. Gao and H. Yan, *Nat. Energy*, 2016, **1**, 16089.
26 H. Mori, S. Jinnai, Y. Hosoda, A. Muraoka, K. Nakayama, A. Saeki and Y. Ie, *Angew. Chem., Int. Ed.*, 2024, **63**, e202412691.
27 K. Wang, S. Jinnai, T. Urakami, H. Sato, M. Higashi, S. Tsujimura, Y. Kobori, R. Adachi, A. Yamakata and Y. Ie, *Angew. Chem., Int. Ed.*, 2024, **63**, e202412691.
28 F. C. Spano, *Acc. Chem. Res.*, 2010, **43**, 429–439.
29 S. Giannini and J. Blumberger, *Acc. Chem. Res.*, 2022, **55**, 819–830.
30 W. C. Zhao, S. S. Li, H. F. Yao, S. Q. Zhang, Y. Zhang, B. Yang and J. H. Hou, *J. Am. Chem. Soc.*, 2017, **139**, 7148–7151.
31 Z. Zheng, E. F. He, J. Wang, Z. T. Qin, T. Q. Niu, F. Y. Guo, S. Y. Gao, Z. F. Ma, L. C. Zhao, X. H. Lu, Q. F. Xue, Y. Cao, G. T. Mola and Y. Zhang, *J. Mater. Chem. A*, 2021, **9**, 26105–26112.
32 G. G. Malliaras, J. R. Salem, P. J. Brock and J. C. Scott, *Phys. Rev. B*, 1999, **59**, 10371.
33 C. Goh, R. J. Kline, M. D. McGehee, E. N. Kadnikova and J. M. J. Fréchet, *Appl. Phys. Lett.*, 2005, **86**, 122110.
34 S. D. Dimitrov and J. R. Durrant, *Chem. Mater.*, 2014, **26**, 616–630.
35 J. L. Wu, F. C. Chen, Y. S. Hsiao, F. C. Chien, P. L. Chen, C. H. Kuo, M. H. Huang and C. S. Hsu, *ACS Nano*, 2011, **5**, 959–967.
36 C. M. Proctor, C. Kim, D. Neher and T. Q. Nguyen, *Adv. Funct. Mater.*, 2013, **23**, 3584–3594.
37 W. Zhao, D. Qian, S. Zhang, S. Li, O. Inganäs, F. Gao and J. Hou, *Adv. Mater.*, 2016, **28**, 4734.
38 A. Yamakata, K. Kato, T. Urakami, S. Tsujimura, K. Murayama, M. Higashi, H. Sato, Y. Kobori, T. Umeyama and H. Imahori, *Chem. Sci.*, 2024, **15**, 12686–12694.
39 K. Wang, S. Jinnai, T. Urakami, H. Sato, M. Higashi, S. Tsujimura, Y. Kobori, R. Adachi, A. Yamakata and Y. Ie, *Angew. Chem., Int. Ed.*, 2024, e202412691.
40 S. Jinnai, K. Murayama, K. Nagai, M. Mineshita, K. Kato, A. Muraoka, A. Yamakata, A. Saeki, Y. Kobori and Y. Ie, *J. Mater. Chem. A*, 2022, **10**, 20035–20047.
41 A. Yamakata, T. Ishibashi and H. Onishi, *Chem. Phys. Lett.*, 2001, **333**, 271–277.
42 A. Yamakata, M. Kawaguchi, N. Nishimura, T. Minegishi, J. Kubota and K. Domen, *J. Phys. Chem. C*, 2014, **118**, 23897–23906.
43 J. I. Pankove, *Optical Processes in Semiconductors*, Dover, 1975.
44 L. Ye, H. W. Hu, M. Ghasemi, T. H. Wang, B. A. Collins, J. H. Kim, K. Jiang, J. H. Carpenter, H. Li, Z. K. Li, T. McAfee, J. B. Zhao, X. K. Chen, J. L. Y. Lai, T. X. Ma, J. L. Bredas, H. Yan and H. Ade, *Nat. Mater.*, 2018, **17**, 253–260.
45 Y. K. Li, Y. Guo, Z. Chen, L. L. Zhan, C. L. He, Z. Z. Bi, N. N. Yao, S. X. Li, G. Q. Zhou, Y. P. Yi, Y. Yang, H. M. Zhu, W. Ma, F. Gao, F. L. Zhang, L. J. Zuo and H. Z. Chen, *Energy Environ. Sci.*, 2022, **15**, 855–865.
46 G. C. Han and Y. P. Yi, *Acc. Chem. Res.*, 2022, **55**, 869–877.
47 G. C. Zhang, X. K. Chen, J. Y. Xiao, P. C. Y. Chow, M. R. Ren, G. Kupgan, X. C. Jiao, C. C. S. Chan, X. Y. Du, R. X. Xia, Z. M. Chen, J. Yuan, Y. Q. Zhang, S. F. Zhang, Y. D. Liu, Y. P. Zou, H. Yan, K. S. Wong, V. Coropceanu, N. Li, C. J. Brabec, J. L. Bredas, H. L. Yip and Y. Cao, *Nat. Commun.*, 2020, **11**, 3943.
48 V. Coropceanu, X. K. Chen, T. H. Wang, Z. L. Zheng and J. L. Brédas, *Nat. Rev. Mater.*, 2019, **4**, 689–707.
49 L. L. Zhan, S. X. Li, Y. K. Li, R. Sun, J. Min, Y. Y. Chen, J. Fang, C. Q. Ma, G. Q. Zhou, H. M. Zhu, L. J. Zuo, H. Y. Qiu, S. C. Yin and H. Z. Chen, *Adv. Energy Mater.*, 2022, **12**, 2201076.
50 F. D. Eisner, M. Azzouzi, Z. P. Fei, X. Y. Hou, T. D. Anthopoulos, T. J. S. Dennis, M. Heeney and J. Nelson, *J. Am. Chem. Soc.*, 2019, **141**, 6362–6374.
51 T. J. Aldrich, M. Matta, W. G. Zhu, S. M. Swick, C. L. Stern, G. C. Schatz, A. Facchetti, F. S. Melkonyan and T. J. Marks, *J. Am. Chem. Soc.*, 2019, **141**, 3274–3287.